

Steering the Topological Defects in Amorphous Laser-Induced Graphene for Direct Nitrate-to-Ammonia Electoreduction

Le Cheng, Tinghao Ma, Binghao Zhang, Libei Huang, Weihua Guo, Feijun Hu, He Zhu, Zhaoyu Wang, Tingting Zheng, Deng-Tao Yang, Chi-Kit Siu, Qi Liu, Yang Ren, Chuan Xia, Ben Zhong Tang, and Ruquan Ye*



Cite This: *ACS Catal.* 2022, 12, 11639–11650



Read Online

ACCESS |



Metrics & More



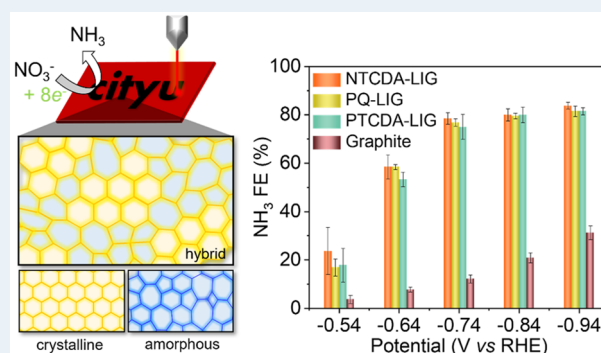
Article Recommendations



Supporting Information

ABSTRACT: Developing metal-free electrocatalysts for direct nitrate-to-ammonia reduction is promising to remediate wastewater yet challenged by the poor ammonia selectivity. Amorphization has become an emerging strategy to afford conventional materials with exotic physical, chemical, and electronic properties. Transient laser heating of polymers produces graphene with an unusual polycrystalline lattice, yet the control of graphene amorphicity is difficult due to the extreme conditions and fast kinetics of the lasing process. Here, we report the synthesis of amorphous graphene with a tailorable heterophase, topologically disparate from crystalline graphene and amorphous carbon. Atomic-resolution imaging reveals the intermediate crystallinity comprising both six-membered rings and polygons, the ratio of which directly correlates with the aromatic structures of the precursors. These amorphous graphenes, as metal-free catalysts, show high performance in direct nitrate-to-ammonia electroreduction. The performance is associated with the amorphicity of graphene and reaches a maximum ammonia Faradaic efficiency of 83.7% at -0.94 V vs reversible hydrogen electrode. X-ray pair distribution functions and paramagnetism disclose the elongated carbon–carbon bonds and rich unpaired electrons in amorphous graphene, which exhibit more favorable adsorption of nitrate as suggested by theoretical calculations. Our findings shed light on the controllable synthesis of graphene with unusual topologies that could find broad applications in electronics, catalysis, and sensors.

KEYWORDS: nitrate reduction, laser-induced graphene, metal-free, topological defects, ammonia synthesis, X-ray pair distribution functions



High nitrate (NO_3^-) concentration in surface water and groundwater has become a ubiquitous environmental problem encountered by the whole world, which poses a threat to public health through entering the food chain and drink water.^{1,2} NO_3^- reduction reaction (NO_3RR) is recently considered as an effective and green technology that not only alleviates growing NO_3^- pollution but also produces harmless or useful nitrogen species.^{3–5} Among the reduction products, ammonia (NH_3) is the most high-value-added, which can serve as essential chemical feedstock, fuel, and fertilizer.^{6,7} By utilizing water and nitrate as the hydrogen and nitrogen source, the electro-synthesizing of NH_3 from NO_3^- is a promising alternative of the traditional energy-intensive Haber-Bosch process.⁸ However, the conversion of NO_3^- to NH_3 involves multiple steps accompanying with eight-electron transfer and needs to compete with the thermodynamically favorable hydrogen evolution reaction (HER). Therefore, developing novel catalysts with high efficiency is of great significance and becoming an important subject in this field. Currently, the mostly explored catalysts for nitrate reduction

are metal containing. Many noble and nonnoble metals, e.g., Pd-doped TiO_2 nanoarray,⁹ Ru-dispersed Cu nanowire,¹⁰ FeOOH nanorod with intrinsic oxygen vacancy,¹¹ Cu/ Cu_2O nanowire arrays,⁵ etc., has been demonstrated to be active for the NO_3RR . However, there are limits for metal-based catalysts, including high cost, easy leaching, and dominant HER under high overpotentials. Previous studies reported that carbon materials could be candidates for nitrate reduction, yet the NH_3 selectivity is minuscule, because the nonmetal electrodes tend to reduce NO_3^- into N_2 and the Faradaic efficiency (FE) toward NH_3 is usually lower than 20%.^{12–14} In this regard, it is highly desired yet challenging to rationally

Received: July 4, 2022

Revised: August 17, 2022

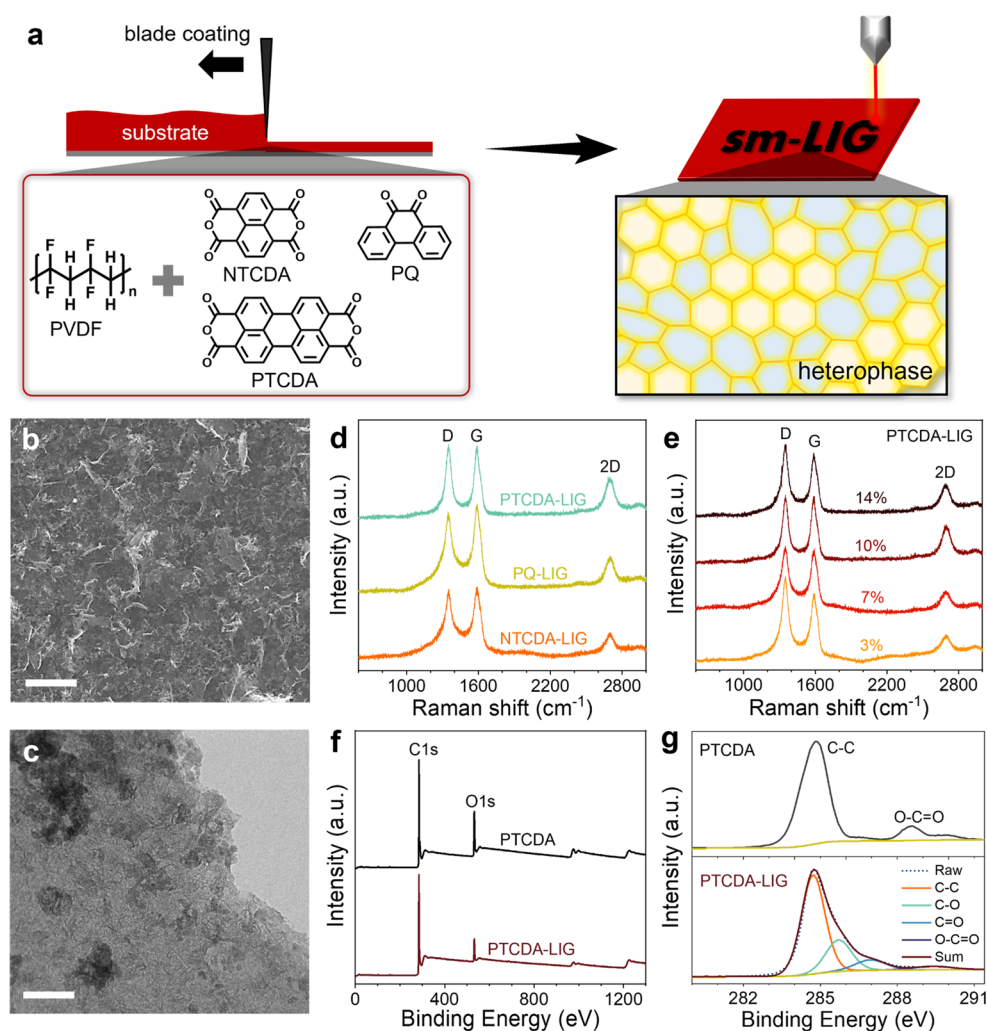


Figure 1. (a) Schematic illustration of the preparation process of sm-LIG. (b) SEM image of PTCDA-LIG; scale bar, 10 μm . (c) TEM image of PTCDA-LIG; scale bar, 100 nm. (d) Raman spectra of NTCDA-, PTCDA-, and PQ-LIG prepared at 10% power and 10 pulses/dot. (e) Raman spectra of PTCDA-LIG prepared under different laser powers (pulse density: 10 pulses/dot). (f) XPS survey spectra and (g) C 1s spectra of PTCDA and PTCDA-LIG.

design and synthesize efficient metal-free electrocatalysts for direct nitrate-to-ammonia reduction.

Amorphization has emerged as an attractive structure engineering strategy to modulate and optimize the physical, chemical, electrical, and mechanical properties of nanomaterials.^{15–17} For example, free-standing monolayer amorphous carbon was reported to be insulating,¹⁵ which is completely opposite to the monolayer graphene with high electron mobility.¹⁸ Compared with the crystalline counterpart, amorphous phase features a long-range disordered atomic arrangement, which offers abundant vacancies and a unique localized electronic structure. Many recent research revealed that materials with amorphous phase or amorphous/crystalline heterophase exhibited significantly enhanced performance in electrocatalytic reactions.^{19–23} For example, the crystalline-to-amorphous transformation of PtSe_x film²¹ and $\text{Pd}_3\text{P}_2\text{S}_8$ nanodot,²² were demonstrated to boost the electrocatalytic activity toward HER. Wang et al. reported that structurally disordered RuO_2 nanosheets displayed high NH_3 FE and selectivity in NO_3RR , greatly outperforming the higher crystallinity samples.²⁴ Based on this, it is expected to enhance the NO_3^- -to- NH_3 reduction performance of nonmetal catalysts by constructing amorphous structures.

Graphene is a typical two-dimensional (2D) carbon material with sp^2 carbon atoms arranged in the form of honeycomb lattice.^{25,26} Methods including the Scotch tape method,²⁶ chemical vapor deposition (CVD),^{27,28} liquid-phase exfoliation,^{29,30} and oxidation–reduction^{31,32} have been developed to produce graphene with traditional crystalline structures mainly composed of six-membered rings. In 2014, the emergence of laser-induced graphene (LIG)^{33–35} demonstrated that transient laser irradiation could be a promising way to conveniently construct an amorphous structure under ambient conditions. Under the abrupt elevation of local temperature ($>2500^\circ\text{C}$) caused by laser irradiation, covalent bonds in carbonaceous precursors are broken and reorganized into graphitic forms, accompanied by the released of gas molecules. Due to the subsequent rapid cooling process, the LIG is frozen in a kinetic state, featuring a unique ultrapolycrystalline structure with abundant pentagons and heptagons rather than the conventional hexagon lattice. Since the discovery, numerous synthetic or naturally occurring polymeric materials have been employed for LIG synthesis,^{33,36–38} The unusual amorphous lattice was thought to contribute to high capacitance because of the high density of defects and states near the Fermi level.³³ In addition, LIG has been widely applied in many applications such as

water treatment,³⁹ disinfection,^{40,41} sensors,^{42–44} and electrocatalysis,^{45,46} owing to the facile synthesis and exotic properties. Literature studies demonstrate that the structure and compositions of LIG largely depend on the utilized precursors.^{36,47} However, it remains challenging to rationally control the amorphous structure of LIG at the atomic level due to the extreme conditions and fast kinetics of the lasing process.

In this work, we report the first successful conversion of small molecules into graphene (sm-LIG) with a tunable amorphous/crystalline heterophase structure by infrared (IR) laser irradiation under ambient conditions. Advanced imaging and spectroscopy techniques reveal the distinct topological structure of sm-LIG. Instead of the conventional hexagonal lattice in graphene or the completely disordered structure in conventional LIG, sm-LIGs contain honeycomb-like nanocrystallites randomly embedded in disordered carbon polygons. The domain sizes of the hexagonal lattice show a positive correlation with the aromatic structure of the precursor molecules. When the amorphicity-controlled sm-LIGs are applied as metal-free catalysts for nitrate reduction, high efficiency of direct eight-electron NO_3^- -to- NH_3 conversion is discovered. X-ray pair distribution functions (PDF) and electron paramagnetic resonance (EPR) unravel the long-range disordered local atomic environment and abundant unpaired electrons in sm-LIGs, which correlate with the NO_3^- -to- NH_3 activities. Further theoretical calculations suggest that these lattice defects account for the activities.

■ RESULTS AND DISCUSSION

The schematic illustration of the preparation process of sm-LIG is demonstrated in Figure 1a. A series of polycyclic aromatic dianhydride or quinone, namely 1,4,5,8-naphthalene-tetracarboxylic dianhydride (NTCDA), 9,10-phenanthrenequinone (PQ), and 3,4,9,10-perylene-tetracarboxylic dianhydride (PTCDA), are selected as precursors. These small molecules were first mixed with polyvinylidene fluoride (PVDF) in *N*-methyl pyrrolidone (NMP) suspensions and then blade coated on aluminum foils to obtain uniform films. After that, the precursor films were treated by IR laser directly to produce sm-LIGs. Here, PVDF serves as the binder of small molecules, and it has been demonstrated to be ablated rather than converted into graphene after laser irradiation.³⁶ Under ambient conditions and using a computer-controlled IR laser, NTCDA, PQ, and PTCDA can be readily converted into sm-LIG with designed patterns (Figure S1). The sm-LIGs prepared with the laser parameter of 10% power (6.0 W) and 10 pulses/dot were further characterized by Raman spectroscopy, scanning electron microscopy (SEM), and transmission electron microscopy (TEM). As shown in the SEM images (Figure 1b, Figure S2a and c), sm-LIGs exhibit porous structures made up of randomly stacked graphene sheets on the microscale because of the rapid release of gaseous products during the laser irradiation process, just like the previously reported LIG.³³ The 2D layered structure as well as typical wrinkles and edges of graphene sheets can be clearly identified in the TEM images (Figure 1c, Figure S2b and d). From the Raman spectra (Figure 1d), three primary signals, i.e., D band at $\sim 1350\text{ cm}^{-1}$, G band at $\sim 1580\text{ cm}^{-1}$, and 2D band at $\sim 2700\text{ cm}^{-1}$, are observed. The very presence of a G band and 2D band, which are induced by in-plane vibrations of sp^2 carbon atoms and second-order zone-boundary phonons,^{48,49} respectively, indicate the successful formation of a graphene

structure. According to the spectra, the $I_{2\text{D}}/I_{\text{G}}$ of NTCDA-LIG, PQ-LIG, and PTCDA-LIG are 0.62, 0.83 and 1.19, respectively. The smaller $I_{2\text{D}}/I_{\text{G}}$ ratio of NTCDA-LIG suggests that it contains thicker stacking than others.^{50,51} The $I_{\text{D}}/I_{\text{G}}$ of NTCDA-LIG, PQ-LIG, and PTCDA-LIG are determined to be 1.31, 1.23, and 1.15, respectively, which suggests a higher graphitization degree of PTCDA-LIG.⁵² The laser-induced conversion process and the chemical structure of sm-LIGs are further revealed by X-ray photoelectron spectroscopy (XPS). The peaks at 284.0 and 530.0 eV in the survey spectra of sm-LIGs and precursor molecules are attributed to the C 1s and O 1s (Figure 1f, Figures S3a and S4a), from which the C/O atomic ratio was calculated and listed in Table S1. Compared with precursor molecules, significant diminishment of O 1s peaks for the sm-LIGs is exhibited; for example, the C/O ratio was 3.71 for PTCDA and 8.08 for PTCDA-LIG, demonstrating massive removal of oxygen after laser irradiation. In addition, the C/O ratio of these three sm-LIGs is essentially the same, which suggests the resemblance of sm-LIGs in chemical components. From the deconvoluted C 1s spectrum shown in Figure 1g, the C 1s signal of PTCDA primarily consists of two peaks, assigned to the carbon in an aromatic perylene core (284.8 eV) and anhydride group (288.5 eV).^{53,54} For PTCDA-LIG, the O–C=O peak (289.5 eV) is dismissed while the C–O (285.8 eV) and C=O (287.1 eV) peaks emerge, which indicates the complete transformation of the anhydride structure to other oxygen-containing functional groups. Similar conclusions can be drawn from the XPS spectra of NTCDA- and PQ-LIG and their precursor molecules (Figures S3b and S4b).

The effect of laser parameters including power and pulse density is systematically investigated with Raman spectroscopy. By fixing the laser power at 3%, it is found that a threshold of pulse density (10 pulses/dot for PQ, 7 pulses/dot for NTCDA and PTCDA) should be reached for the successful formation of sm-LIGs with a clear D band, G band, and 2D band (Figure S5a, c, and e). When the pulse density is fixed at 10 pulses/dot, the regular appearance of a 2D peak demonstrates that direct laser scribing can readily transform these small molecules into graphene-like structures within a wide range of laser powers (Figure 1e, Figure S5b and d). Taking PTCDA as an example, with the increase of laser power from 3% to 10%, the 2D band exhibits an evident enhancement of intensity and narrowing of full width at half-maximum (fwhm; Figure 1e), demonstrating a reduced layer stacking thickness and improved quality of graphene structures. Yet the further increase in power results in a higher D band and lower 2D band, suggesting the degradation of quality. Overall, when the laser power and pulse density are set at 10% (6.0 W) and 10 pulses/dot, respectively, the resulting sm-LIGs reach optimized qualities. Thus, this parameter is chosen as the default setting for sm-LIG preparation in this work unless otherwise specified.

In addition, the lasing atmosphere was further controlled to explore the mechanism of the laser-induced conversion process. Using PTCDA as the model molecule, it is found that no high-quality graphene could be obtained under N_2 regardless of the laser power (Figure S6a). Then, we conducted the lasing process by finely tuning the atmosphere O_2/N_2 ratio for this molecule (Methods). When O_2 increases from 0 to 20 vol%, the D peak decreases and the 2D peak increases, indicating the improved quality of the graphene structure. Yet when the O_2 concentration is higher than 30 vol %, the graphene structure deteriorates (Figure S6b), due to the

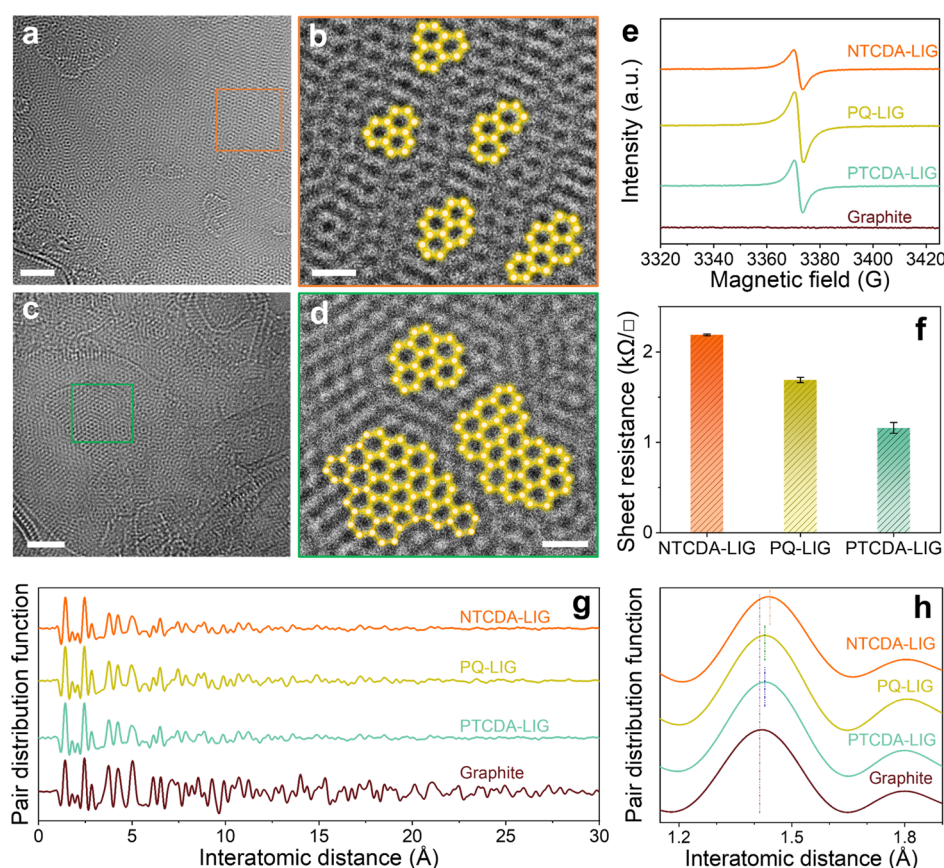


Figure 2. HRTEM images of (a) NTCDA-LIG and (c) PTCDA-LIG; scale bars, 2 nm. Enlargement of indicated area of (b) NTCDA-LIG and (d) PTCDA-LIG; scale bars, 0.5 nm. The domains of six-membered rings are outlined. (e) EPR spectra of sm-LIGs and graphite reference. (f) Sheet resistance of sm-LIGs. (g, h) PDFs of sm-LIGs and graphite reference.

vigorous oxidation reaction with excessive oxygen. These results indicate the crucial role of oxygen in the formation and quality optimization of sm-LIG. Gas products of the laser irradiation process are further monitored by coupling an online mass spectrometer (MS) with the lasing chamber (Figure S7a and Methods). Purified air is utilized as the carrier gas as well as the lasing environmental gas. As shown in the relative content variation profile (Figure S7b), massive CO_2 is released after the laser irradiation, and an obvious ascent of H_2O is detected simultaneously. The release of CO_2 and H_2O proposes that oxygen may play a role in assisting the dehydrogenation and decarboxylation of the small molecules. These reactions may generate carbon radicals to form carbon–carbon bonds and integrate the aromatic rings into a larger conjugated structure, thus they are conducive for graphene formation. Based on the above speculation, another small molecule, perylene, which possesses an identical aromatic ring to that of PTCDA but without oxygenated groups (the molecular structures are depicted in Figure S8), is selected to prepare sm-LIG through the same process. Similarly, the graphene structure formed after lasing in air, while no graphene formed in N_2 (Figure S9). From the results of the atmosphere-controlled experiment (Figure S10), the 2D band starts to appear only when the O_2 concentration reaches 20 vol % and then continues to grow up to an optimal O_2 content of 60 vol%. Further increasing the O_2 concentration to above 60 vol% will burn the perylene with no products left. Compared with PTCDA, it can be concluded that higher O_2 concentration is needed to prepare high-quality LIG from

peryene. The main reason is suggested to be that the intramolecular carbonyl oxygen atoms of PTCDA can also participate in the dehydrogenation and decarboxylation process, as confirmed by the significant decrease of oxygen contents after the formation of PTCDA-LIG (Figure 1f).

To delve into the topology, the nanostructures of sm-LIG are further studied by high-resolution transmission electron microscopy (HRTEM). As shown in the HRTEM images of NTCDA-LIG (Figure 2a), PTCDA-LIG (Figure 2c), and PQ-LIG (Figure S11a), carbon atoms are all arranged in a partially ordered fashion to form graphene planes. To be precise, small domains of six-membered rings are connected by non-six-membered ring carbon (five-, seven-, and eight-membered rings). This means that the sm-LIG features an intermediate structure between amorphous and crystalline; both ordered honeycomb-like crystallites and disordered amorphous regions coexist within one graphene layer. For comparison, graphite and polyimide-induced LIG (PI-LIG) were selected as a reference. Distinctly, the carbon atoms in the graphite plane are highly ordered, and the lattices are all comprised of regular hexagons without bending or distortion (Figure S12), which indicates the highly crystalline structure. In contrast, PI-LIG exhibits an almost completely disordered structure; most of the carbon atoms are in the form of pentagons and heptagons (Figure S13), which is in accordance with the previous report.³³ The nanostructure difference is further revealed by electron paramagnetic resonance (EPR) spectra. As shown in Figure 2e, three sm-LIGs exhibit a characteristic symmetric peak with $g = 2.003$, which is assigned to the free electrons

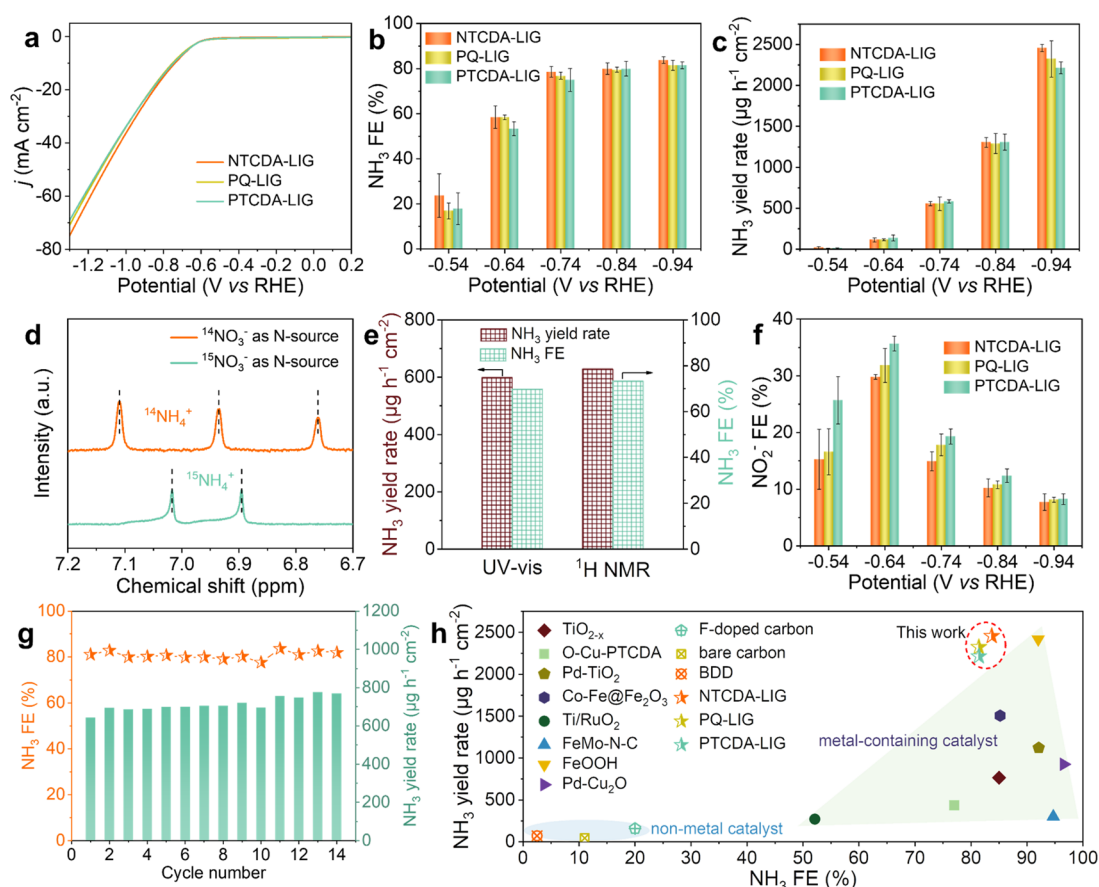


Figure 3. (a) Electrochemical activity of NO₃RR over HER. Solid lines are LSV curves of sm-LIGs in 1 M NaNO₃, while dashed lines are LSV curves in 1 M NaCl (scan rate: 10 mV s⁻¹). (b) NH₃ FE and (c) NH₃ yield rate of sm-LIGs at different potentials. (d) ¹H NMR spectra of electrolytes after the NO₃⁻ reduction using ¹⁴NO₃⁻ and ¹⁵NO₃⁻ as a N source. (e) The NH₃ FE and yield rate calculated by ¹H NMR and indophenol blue method. (f) NO₂⁻ FE of sm-LIGs at different potentials. (g) NH₃ FE and yield rate of NTCDA-LIG at -0.74 V vs RHE in different cycles. (h) Comparison of the NH₃ FE and yield rate with reported electrocatalysts (see Table S3 for detailed references).

trapped by oxygen vacancies.^{55,56} The difference in peak intensity could be attributed to the slightly different oxygen content of the sm-LIGs. On the contrary, no EPR signal was detected for the graphite reference. This result suggests more lattice defects and unpaired electrons in the sm-LIG,^{57,58} which is consistent with the HRTEM characterization. The more careful analysis of the atomic structure reveals that the intermediate crystal structure of sm-LIGs appeared to be correlated with the molecular structure of precursors (Figure 2b,d, Figure S11b). It could be observed that the crystallites in PTCDA-LIG are larger than that in PQ- and NTCDA-LIG, probably because of the larger pristine aromatic rings in the PTCDA molecule. In addition, the crystalline size (L_a) along the a axis could be calculated according to the Raman results (Figure 1d) through equation $L_a = (2.4 \times 10^{-10}) \times \lambda_1^4 \times (I_G/I_D)$, where λ_1 is the wavelength of the Raman laser (514 nm).⁵⁹ The I_D/I_G and corresponding L_a value was determined to be 1.31 (12.79 nm), 1.23 (13.62 nm), and 1.15 (14.57 nm) for NTCDA-, PQ-, and PTCDA-LIG, respectively, which is in accordance with the HRTEM observation. Accordingly, the sheet resistance shows a decreasing tendency with the increase of the domain size of six-membered rings (Figure 2f). These results further proved that the ratio of the crystallites and amorphous region of sm-LIGs is affected and determined by the aromatic structures of precursors. The underlying mechanism can be speculated to be that the six-membered

rings in sm-LIGs are mainly originated from the precursors, while the polygons result from the rearrangement of atoms under the high temperature induced by the laser.

In addition, pair distribution functions (PDFs) of sm-LIGs and the graphite reference are evaluated to further study their global atomic configuration information. As shown in Figure 2g, all of the samples exhibit nearly the same peak position, with the nearest neighbor distances and next-nearest neighbor distances of ~ 1.4 Å and ~ 2.5 Å, respectively, which accord with the literature.^{15,60} Apparent subpeaks in the longer interatomic-distance ranges of graphite indicate a typical crystalline feature. Yet the weakening or broadening of these peaks in sm-LIGs (Figure 2g) and PI-LIG (Figure S14) represents a lower long-range order, which proves the presence of amorphous structures. A closer look at the first peak position (Figure 2h) shows that the bond distance of graphite is 1.42 Å, which shifted to a longer distance for sm-LIGs. Among them, NTCDA-LIG shows an even longer bond distance (1.44 Å) than that of PTCDA-LIG (1.43 Å) and PQ-LIG (1.43 Å), possibly due to the most abundant polygons as confirmed by the HRTEM and Raman spectra. The comparison between sm-LIGs and their corresponding precursors is shown in Figure S15. The precursor molecules only possess two prominent peaks corresponding to the polycyclic aromatic rings, and the indistinguishable subpeaks at longer distances indicate the total absence of long-range order.

After laser irradiation, there emerge enhanced subpeaks, indicating the formation of partially ordered structures. In addition, the primary peaks locate at a longer distance for all of the sm-LIGs (Figure S15b), suggesting different atomic environments between sm-LIGs and small molecules.

The nitrate reduction reaction (NO_3RR) catalyzed by these three sm-LIGs was conducted in a homemade H-type cell. The catalytic activity was first evaluated by the linear sweep voltammetry (LSV) curves recorded in 1 M NaNO_3 (solid lines in Figure 3a). Blank LSV curves were measured in 1 M NaCl (dash lines in Figure 3a) for reference. For all of the sm-LIG electrodes, the significantly higher current densities in the presence of NO_3^- indicate the occurrence of NO_3^- reduction. These three catalysts show a very close sharp onset at a potential of -0.6 V vs a reversible hydrogen electrode (RHE). Among them, NTCDA-LIG exhibits the highest current density at different potentials from -0.65 V to -1.3 V vs RHE, suggesting better catalytic activity for NO_3^- reduction. Following NTCDA-LIG, the current density drops slightly for PQ- and PTCDA-LIG. Furthermore, electrochemical impedance spectroscopy (EIS) was recorded during the electrochemical test. These sm-LIG electrodes show similar internal resistance (R_Ω), yet NTCDA-LIG demonstrates a smaller Nyquist semicircle diameter (i.e., the charge-transfer resistances, R_{ct}) than the other two (Figure S16), also indicating faster charge-transfer kinetics for the NO_3^- reduction.

Next, Faradaic efficiency (FE) toward the target reduction product (NH_3) and the byproduct (NO_2^- and H_2) are calculated based on 1-h chronoamperometry tests at different potentials (Figure S17). The concentrations of NH_3 and NO_2^- in the postelectrolytes were quantified according to colorimetric methods (see calibration curves in Figures S18 and 19). The gas product H_2 was detected by an online gas chromatograph equipped with a thermal conductivity detector. According to the calculated FE (Figure 3b,f and Figure S20), it is found that almost under each applied potential, NH_3 is the dominant reduction product over NO_2^- . For all of the catalysts, the NH_3 FE and yield rate increase continuously over the applied voltage. However, the NO_2^- FE first increases from -0.54 to -0.64 V vs RHE and then decreases. The total FE toward NH_3 and NO_2^- reaches 93–95% for these catalysts, which suggests that the competitive hydrogen production is brutally suppressed. Accordingly, the H_2 FE of the sm-LIGs is relatively low, with the lowest value of only 0.5% at -0.74 V vs RHE, 0.4% at -0.84 V vs RHE, and 0.7% at -0.74 V vs RHE for NTCDA-, PQ- and PTCDA-LIG, respectively. By comparing the NH_3 FE (Figure 3b) and yield rate (Figure 3c) at each given potential, it can be concluded that NTCDA-LIG shows better NO_3^- reduction performance especially at higher potentials, reaching a maximum NH_3 FE of 83.7% and yield rate of $2456.8 \mu\text{g h}^{-1} \text{cm}^{-2}$ at -0.94 V vs RHE. In comparison, PQ-LIG and PTCDA-LIG demonstrate a slightly lower NH_3 FE and a yield rate of 81.43% ($2324.1 \mu\text{g h}^{-1} \text{cm}^{-2}$) and 81.44%, ($2214.5 \mu\text{g h}^{-1} \text{cm}^{-2}$) at -0.94 V vs RHE, respectively. While the selectivity of NO_2^- and H_2 is basically in the reverse order. Almost under each applied potential, PTCDA-LIG shows a higher NO_2^- FE (Figure 3f) and yield rate (Figure S21) as well as H_2 FE (Figure S20) than PQ-LIG, then followed by NTCDA-LIG. In addition, the electrochemical active surface area (ECSA) of these three sm-LIGs was evaluated by the electrochemical double layer capacitance (C_{dl}) method. Cyclic voltammetry (CV) curves under different scan rates from 20 to 120 mV s^{-1} were recorded (Figure S22),

from which the C_{dl} were calculated to be 1.79, 3.11, and 3.80 mF cm^{-2} for NTCDA-, PQ-, and PTCDA-LIG, respectively. The smaller C_{dl} of NTCDA-LIG could be related to the thicker stacking, as suggested by the smaller I_{2D}/I_G ratio in the Raman spectra (Figure 1d).^{50,51} After normalized by ECSA, the LSV curves and NH_3 yield rate of NTCDA-LIG exhibit more obvious superiority than PQ-LIG and PTCDA-LIG (Figure S23), which further suggests its better intrinsic activity in the direct NO_3^- -to- NH_3 electroreduction.

To confirm the source of NH_3 and the accuracy of the colorimetric method, isotopic labeling and quantitative nuclear magnetic resonance (NMR; see calibration curve in Figure S24) were performed. Only a triplet of $^{14}\text{NH}_3$ and a doublet of $^{15}\text{NH}_3$ in the ^1H NMR spectrum can be observed in the ^1H NMR spectra when $^{14}\text{NO}_3^-$ and $^{15}\text{NO}_3^-$ are used as the nitrate source, respectively (Figure 3d), indicating that the produced NH_3 do originated from the nitrate in the electrolyte. Moreover, the NH_3 Faradaic efficiency and yield rate calculated through the quantitative NMR method are in good accordance with that by the colorimetric method (Figure 3e), which ensures the accuracy and reliability of the results. We also analyzed the NH_3 FE and yield rate along with the electrolysis time using NTCDA-LIG at -0.74 V vs RHE (Figure S25). It is observed that the NH_3 FE and yield rate are lower at the first 15 min, only reaching 66.7% and $449 \mu\text{g h}^{-1} \text{cm}^{-2}$. With the extension of electrolysis time to more than 30 min, the NH_3 FE and yield rate gradually increased to $\sim 80\%$ and $580 \mu\text{g h}^{-1} \text{cm}^{-2}$. A similar phenomenon has been reported, and it was suggested that the accumulated NO_2^- in electrolyte would suppress the desorption of $^*\text{NO}_2$ and promote the overall NO_3^- -to- NH_3 reduction.⁶¹

In combination with the topological structure of sm-LIGs, the higher intrinsic activity of NTCDA-LIG in direct NO_3^- -to- NH_3 electroreduction may be ascribed to the most abundant amorphous structures. Therefore, the performance was further compared with pyrolytic graphite consisting of carbon atoms arranged in regular hexagons. The Raman spectrum and TEM image of pyrolytic graphite are shown in Figure S26. As expected, the FE toward NO_2^- is overwhelming compared to that toward NH_3 under each potential (Figure S27). The maximum NH_3 Faradaic efficiency and yield rate could only reach 31.3% and $250.5 \mu\text{g h}^{-1} \text{cm}^{-2}$ at -0.94 V vs RHE, which is close to the previously reported value.¹² This result further suggests the function of amorphous structure in promoting the performance of direct NO_3^- -to- NH_3 electroreduction. We further compare the sm-LIGs to other nonlaser-induced carbon materials, including commercially available carbon black (CB; Vulcan XC-72R, Fuel Cell Store) and thermally annealed NTCDA (NTCDA-annealed; Methods). Both samples show broad D peaks and negligible 2D peaks in the Raman spectra (Figure S28), which are different from those of sm-LIGs. Figure S29 shows the ammonia FEs and yield rate of CB and NTCDA-annealed. Both samples show inferior performance compared to sm-LIGs, especially at high overpotentials. The maximum NH_3 FE and yield rate of CB is 51.0% and $636.2 \mu\text{g h}^{-1} \text{cm}^{-2}$, which is only 60% and 25% of that of NTCDA-LIG.

Additionally, we further investigate the defect effect on nitrate reduction using a series of PTCDA-LIGs with different $I_D:I_G$ ratios prepared by altering the laser parameters (Methods). These samples were denoted as PTCDA-LIG-1.77, PTCDA-LIG-1.15, and PTCDA-LIG-0.54, the suffix in which is the I_D/I_G ratio (Figure S30). Among these three

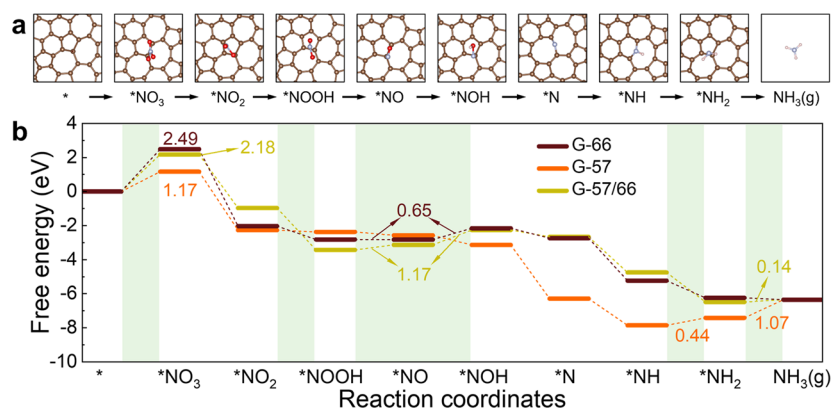


Figure 4. (a) Optimized structures of intermediates on the G-57 site. (b) Gibbs free energy diagrams of different intermediates over G-66, G-57, and G-57/66 sites.

PTCDA-LIGs, PTCDA-LIG-1.15 exhibits the strongest current density, suggesting the highest catalytic activity. The NH_3 FE increases from 74.0% for PTCDA-LIG-0.54 to 80.0% for PTCDA-LIG-1.15 and 82.9% for PTCDA-LIG-1.77. Simultaneously, the NO_2^- FE shows a decreased trend (Figure S31). These results further indicate that defects or amorphous structures benefit the direct NO_3^- -to- NH_3 electroreduction with improved selectivity. Nonetheless, the highest NH_3 yield rate is reached by PTCDA-LIG-1.15 with the modest I_D/I_G because of the proper defect concentration, which provides abundant active sites while maintaining the good conductivity. The influence of oxygen content on the performance is also considered. PQ-LIG was subjected to the post-treatment of H_2O_2 oxidation or thermal reduction (Methods), and the resultant samples are noted as PQ-LIG-A and PQ-LIG-O, respectively. The oxygen contents are measured to be 11.74% for PQ-LIG, 6.43% for PQ-LIG-A, and 18.66% for PQ-LIG-O by XPS (Table S2). As shown in Figure S32, compared with original PQ-LIG, the current densities are smaller for both PQ-LIG-A and PQ-LIG-O. With the increase of oxygen content, the FE exhibits an evident uptrend toward NH_3 (from 76.6% for PQ-LIG-A to 82.7% for PQ-LIG-O) and downward trend toward NO_2^- (from 8.9% for PQ-LIG-A to 4.5% for PQ-LIG-O). The increased selectivity toward NH_3 suggests that higher oxygen content might bring more defect sites and facilitate the NO_3^- -to- NH_3 conversion. The excessive oxygen content will lead to a decay of yield rate and current density, which may be due to the destruction of conductive structures. Nonetheless, NTCDA-, PQ-, and PTCDA-LIG possess very close oxygen content ($\sim 11\%$), thus their performance difference should be ascribed to the amorphicity variation.

To probe the durability of sm-LIGs, stability test was performed on NTCDA-LIG at -0.74 V vs RHE for 14 consecutive electrolysis cycles, each with refreshed electrolyte and lasting 30 min. The current density keeps relatively steady at ~ 11 mA with a slight increase (Figure S33), which may be attributed to the improved wettability of the catalyst. The NH_3 FE and yield rate show negligible decay over the whole test, implying favorable stability of the catalyst in NO_3RR (Figure 3g). Figure 3h displays a comparison of the NH_3 FE and yield rate between the sm-LIG electrodes with some previously reported electrocatalysts. Notably, the nitrate reduction performance of sm-LIGs is much better among metal-free catalysts in terms of NH_3 FE and yield rate. Previously reported nonmetal catalysts often reduce nitrate to N_2 , and the NH_3 FE and yield are usually lower than 20% and $200 \mu\text{g h}^{-1}$

cm^{-2} .^{12–14} For metals, there are reported catalysts with high current density and yield rate; for example, the Pd-doped TiO_2 nanoarray delivers a NH_3 FE of 92.1% and a yield of $1122 \mu\text{g h}^{-1} \text{cm}^{-2}$.⁹ A FeOOH nanorod with intrinsic oxygen vacancy gives a NH_3 FE and yield of 92% and $2419 \mu\text{g h}^{-1} \text{cm}^{-2}$.¹¹ Recently, Chen et al. demonstrated that Ru-dispersed Cu nanowires can reach a high NH_3 FE of 93% and yield above $70\,000 \mu\text{g h}^{-1} \text{cm}^{-2}$ under an industrially relevant nitrate reduction current.¹⁰ By comprehensive comparison, in this work, both high NH_3 FE and yield rate could be reached by sm-LIGs, greatly outperforming reported nonmetal catalysts, and are superior to some of the metal-containing catalysts, which makes it a promising metal-free electrocatalyst in the water pollution treatment and NH_3 green synthesis. It should be noted that metallic catalysts tend to possess lower overpotentials than nonmetals (Table S3), on account of the stronger metal–adsorbate interactions. However, usually the peak NH_3 FE and yield rate cannot be achieved simultaneously by metal catalysts for the fact that the competitive HER will dominate with the increase of the potential for some metals. In comparison, sm-LIGs can maintain the high FE at a high overpotential, which could be an advantage, considering that the current density increases with potential. In addition, the laser technology enables the direct writing of electrodes, which will help the construction of smart agriculture system by coupling with an ammonia sensing LIG electrode for the on-site synthesis and detection of ammonia.

Besides, to delve into the mechanism of nitrate reduction over a disordered carbon plane, density functional theory (DFT) calculations were employed (Methods). The electrochemical reduction of NO_3^- into NH_3 could be divided into a series of elementary deoxidation and hydrogenation reactions ($^*\text{NO}_3^-$ - $^*\text{NO}_2$ - $^*\text{NOOH}$ - $^*\text{NO}$ - $^*\text{NOH}$ - $^*\text{N}$ - $^*\text{NH}$ - $^*\text{NH}_2$ - NH_3).^{9,61} Based on the characterization results, a model of graphene consisting of six-membered ring domains and amorphous domains is established. The corresponding Gibbs free energy of each reaction intermediate is calculated over the sites that were crystalline (G-66) and amorphous (G-57) and the boundary of these two domains (G-57/66). The optimized structures of intermediates on these three sites are displayed in Figure 4a and Figures S34 and S35. As shown in the Gibbs free energy diagrams in Figure 4b, NO_3^- ions are first adsorbed on the surface of graphene to form $^*\text{NO}_3$ with a free energy uphill on all sites. G-57 shows a significantly lower energy barrier of 1.17 eV than those of G-66 and G-57/66, which are 2.49 and 2.18 eV, respectively. This result indicates that the G-57 site is

more favorable for NO_3^- adsorption. Then, the step-by-step split of $^*\text{NO}_3$ to form $^*\text{N}$ and the subsequent hydrogenation of $^*\text{N}$ to $^*\text{NH}$ over G-57 is entirely spontaneous. After that, from $^*\text{NH}$ to $^*\text{NH}_2$ and $^*\text{NH}_2$ to NH_3 , the free energy increased by 0.44 and 1.07 eV, respectively. As for G-66 and G-57/66, there exist ΔG uphill from $^*\text{NOOH}$ to $^*\text{NO}$ and further to $^*\text{NOH}$, totally 0.65 eV for G-66 and 1.17 eV for G-57/66, which will impede the subsequent reactions and increase the yield of NO_2^- . On the basis of the above analysis, the rate-limiting steps for these three sites are all the adsorption of NO_3^- , and G-57 demonstrates the lowest energy barrier. The relatively favorable NO_3^- adsorption of G-57 highlights the significant role of topological defects in initiating the nitrate reduction.

CONCLUSIONS

We have achieved the direct conversion of small aromatic molecules into graphene via a facile laser irradiation method under ambient conditions. Atomic electron microscopy and X-ray PDFs reveal the unique intermediate crystalline structure of sm-LIG, which fills the gap between single-crystalline graphene and amorphous carbon. This intermediate crystalline LIG structure can be controlled by selecting precursors of different aromaticities, resulting in a tunable size of six-membered ring domains and polygonal regions. Benefiting from the most defective structures, the highest NH_3 FE (83.7%) and yield rate ($2456.8 \mu\text{g h}^{-1} \text{cm}^{-2}$) could be reached when using NTCDA-LIG as the electrode in electrochemical nitrate reduction applications. This work provides insight into the controllable synthesis of unconventional amorphous graphene structures and could be instructive for the design and synthesis of high-efficiency nonmetal electrocatalysts.

METHODS

Materials and Chemicals. NTCDA, PTCDA, PQ, perylene, salicylic acid, benzoic acid, sodium citrate ($\text{C}_6\text{H}_5\text{O}_7\text{Na}_3$), and sodium nitroferrocyanide dihydrate ($\text{C}_5\text{FeN}_6\text{Na}_2\text{O} \cdot 2\text{H}_2\text{O}$) were supplied by Aladdin Reagent Ltd. PVDF, NMP, sulfanilamide, phosphoric acid (H_3PO_4 , 85 wt%), and N-(1-naphthyl) ethylenediamine dihydrochloride were purchased from J&K Scientific Ltd. Sodium hypochlorite standard solution (NaClO , 0.1 M), hydrogen peroxide (H_2O_2 , 30 wt%), and sodium hydroxide (NaOH) were bought from Macklin Biochemical Technology Ltd. Sodium nitrate (NaNO_3), sodium nitrite (NaNO_2), and ammonium chloride (NH_4Cl) were provided by Sigma-Aldrich. Pyrolytic graphite powder was purchased from Nanjing XFNANO Materials Tech Co., Ltd. All chemicals and reagents were used as received unless otherwise specified. Deionized (DI) water used was obtained from Milli-Q Plus System.

Fabrication of sm-LIGs. First, PVDF was dissolved in NMP at room temperature to obtain PVDF/NMP solution with different concentrations (3, 4, 6 wt%), to which a certain amount of small molecules were added (NTCDA and PQ to 4 wt% solution, PTCDA, and perylene to 3 wt% solution, respectively). Different concentrations were aimed at ensuring an appropriate viscosity of the mixture for subsequent blade coating, while the mass ratio of PVDF and small molecule was always constant at 1:4. The mixtures were magnetically stirred for 24 h to form uniform suspensions and then bladed into thin films on aluminum foils (the coating thickness was set as 250

μm) followed by 12 h of drying at 80 °C. Laser ablation was conducted on a 10.6 μm CO_2 laser marking machine (Minsheng Laser #MSDB-FM60 CO_2 Laser Marker, 60 W) with a beam size of $\sim 120 \mu\text{m}$, and the laser frequency, speed, and line space were set as 10 kHz, 1000 mm s^{-1} , and 0.03 mm, respectively. The laser power and pulse density were varied from 3% to 14% (i.e., 1.8 to 8.4 W) and 5 to 14 pulses/dot, respectively. The as-prepared LIG was denoted as precursor-LIG. PTCDA-LIG with a higher I_D/I_G was prepared using 3% power and 10 pulses/dot. Lower I_D/I_G PTCDA-LIG was fabricated by two lasing scans with 3% power and 5 pulses/dot. Except for Raman spectroscopy and SEM observation, sm-LIGs were scraped off, washed (NTCDA- and PQ-LIG by NMP, ethanol and DI water, PTCDA-LIG by 1 M KOH and DI water), and dried at 80 °C for further use. PQ-LIG-A was obtained by thermal annealing of PQ-LIG at 750 °C for 2 h in an Ar atmosphere. PQ-LIG-O was prepared by dispersing PQ-LIG in 30 wt% H_2O_2 (0.1 mg/mL) followed by 1 h of sonication and 3 h of agitating at 60 °C. For comparison, NTCDA/PVDF mixed powder (mass ratio 1:4) was annealed at 800 °C for 2 h in an Ar atmosphere for prepared nonlaser-induced samples.

Characterization. Raman spectra were collected on a LabRAM HR800 Laser Confocal Micro-Raman Spectrometer with an excitation wavelength of 514 nm. SEM micrographs were obtained using a QUATTRO S scanning electron microscope with an operating voltage of 10 kV. TEM images were taken using a FEI/Philips Tecnai 12 BioTWIN transmission electron microscope with an acceleration voltage of 120 kV. HRTEM images were recorded using a Themis Z microscope operated at 200 kV. XPS and EPR data were measured using a PHI Quantera SXM scanning X-ray microprobe and an X-band Bruker A300 spectrometer under ambient conditions. Sheet resistance was measured with an HMS-5300 Hall effect measurement system. The PDFs were extracted from high energy synchrotron X-ray total scattering by direct Fourier transform of a reduced structure function ($F(Q)$, up to $Q \approx 24.7 \text{ \AA}^{-1}$) using the 11-ID-C beamline at the Advanced Photon Source (APS) of Argonne National Laboratory (X-ray wavelength 0.1173 \AA). For each sample, the powder was loaded into a 2 mm capillary with data acquisition time of 15 min. The background scattering from the empty capillary was extracted. $G(r)$ functions, $G(r) = 4\pi r[\rho(r) - \rho_0]$, where $\rho(r)$ and ρ_0 are the local and average atomic number densities, were computed with PDFgetX3 software.

Controlled Atmosphere Lasing and Online Analysis of Gas Products. A closed steel chamber with a ZnSe window on top was used to provide specific lasing atmospheres. Different O_2 concentrations were realized by mixing O_2 and N_2 with controlled flow rates. Analysis of gas products was conducted using the controlled atmosphere chamber coupled to a Hiden Analytical mass spectrometer. There are two routes jointed by T-junctions between the carrier gas source and the MS, either passing through (route 1) or in parallel to (route 2) the chamber. In a typical testing process, at the beginning, both routes 1 and 2 were unblocked to let the carrier gas fully fill the system for 20 min. Then, the T-junction was switched to close route 1 and laser scribing conducted in the sealed chamber. After the lasing process and cooling down for 20 min, the gas route was switched from route 2 to route 1 so that the gas products in the chamber could be detected by MS. Here, clean

air was used as the carrier gas for PTCDA lasing, and the gas velocity was kept stable at 20 sccm.

Electrochemical Test. For the preparation of the working electrode, 10 mg of as prepared sm-LIG powder or as received pyrolytic graphite powder was dispersed in 1000 μL of 5 wt% Nafion solution (Sigma-Aldrich, Nafion 117) by 1 h ultrasonication to form uniform ink. Commercially available A4 printing paper was coated with a layer of Au using a BAL-TEC SCD 050 Sputter Coater (current: 60 mA, sputter time: 120 s) and then cut into discs with a diameter of 17 mm. Subsequently, 100 μL of the ink was drop-casted on the Au coated discs and dried naturally overnight. The catalyst loading was calculated to be 0.44 mg cm^{-2} . Electrochemical nitrate reduction was carried out in a homemade H-type cell using a CHI650E electrochemical workstation. Three-electrode configuration was adopted, consisting of a sm-LIG working electrode, a Ag/AgCl reference electrode, and a platinum (Pt) foil counter electrode. The effective working area of both working and counter electrodes was 1 cm^2 . Nafion-117 membrane was assembled to separate the cathode and anode compartments, and each compartment was added with 1.75 mL of 1 M NaNO_3 aqueous solution as an electrolyte. The calibration of the reference electrode was carried out according to the previously reported method.^{62,63} All applied potentials were converted to the RHE scale via the following equation: $E(\text{vs RHE}) = E(\text{vs Ag/AgCl}) + 0.0592 \text{ pH} + 0.250 \text{ V}$. The resistance between the reference and working electrode was measured by EIS by applying an AC voltage in the frequency range between 1000 kHz and 0.1 Hz at a potential of 0.06 V vs RHE and manually compensated. LSV curves were collected at a scan rate of 10 mV s^{-1} from +0.66 V to -1.34 V vs RHE , and chronoamperometry tests were performed at -0.54 , -0.64 , -0.74 , -0.84 , and -0.94 V vs RHE for each sample for 1 h duration. All of the electrochemical nitrate reduction tests were repeated three times to ensure reliability.

Quantification of Products and Calculation of FE. During the chronoamperometry test, high purity Ar was bubbled into the cathode chamber as a carrier gas at a flow rate of 5 sccm. The produced H_2 was quantified by an online gas chromatograph (Ruimin GC 2060, Shanghai) equipped with a thermal conductivity detector. The FE of H_2 was calculated using the following equation:

$$\text{FE}_{\text{H}_2}(\%) = \frac{Q_{\text{H}_2}}{Q_{\text{total}}} \times 100\% = \frac{\left(\frac{\nu}{60 \text{ s/min}} \right) \times \left(\frac{V_{\text{H}_2}}{22400 \text{ cm}^3/\text{mol}} \right) \times N \times F}{j} \times 100\%$$

where ν is the carrier gas flow rate (5 sccm), N is the number of electrons needed to form a molecule of H_2 ($2e^-$), F is the Faraday constant (96485 C mol^{-1}), and j is the recorded current density.

After each chronoamperometry test, the electrolytes were collected for liquid product detection. The main products, HN_3 and nitrite NO_2^- , were quantitatively analyzed using colorimetric methods reported elsewhere^{64,65} using a Shimadzu-UV1700 spectrometer. The indophenol blue method and Griess test were applied for the detection of HN_3 and NO_2^- , respectively. For the determination of HN_3 , reagent A (1 M NaOH solution containing 5 wt% salicylic acid and 5 wt% sodium citrate) and reagent B (mixture of 5 mL of 0.05 M

NaClO solution and 1 mL of 1 wt% $\text{C}_5\text{FeN}_6\text{Na}_2\text{O}$ solution) were freshly prepared as the chromogenic indicator. 200 μL of electrolyte was mixed with 200 μL of reagent A and 100 μL of reagent B. After 1 h, the absorption spectra were measured by adding 0.4 mL of the above mixture with 2.6 mL of H_2O . The absorbance at $\lambda = 650 \text{ nm}$ was used to calculate the NH_3 concentration. To determine NO_2^- , Griess reagent was prepared by dissolving 0.1 g of N-(1-naphthyl) ethylenediamine dihydrochloride, 1.0 g of sulfonamide, and 2.94 mL of H_3PO_4 (85 wt%) in 50 mL of H_2O . 500 μL of electrolyte was mixed with 1 mL of water followed by the addition of 500 μL of Griess reagent. After 10 min, the absorption spectra were measured by adding 1.0 mL of the above mixture with 2.0 mL of H_2O . The absorbance at $\lambda = 540 \text{ nm}$ was used to calculate the NO_2^- concentration. The calibration curves were obtained through the same operation using a series of NH_4Cl and NaNO_2 standard solutions with known concentrations. In some cases, the electrolyte was diluted to ensure that the measured concentration was in the range of calibration curves. FE was calculated via the following equation:

$$\text{FE}(\%) = \frac{Q_{\text{product}}}{Q_{\text{total}}} \times 100\% = \frac{C \times V \times N \times F}{Q_{\text{total}}} \times 100\%$$

where C is the detected concentration of NH_3 or NO_2^- in the electrolyte, V is the volume of the electrolyte, N is the electrons needed to form a molecule of NH_3 ($8e^-$) or NO_2^- ($3e^-$), and Q_{total} is the total charge transferred during the chronoamperometry test.

NMR and Isotopic Labeling Experiment. The concentration of NH_3 was also confirmed by a quantitative NMR method using benzoic acid as the interior label. The NMR spectra were collected by a Bruker AVANCE III 300 MHz spectrometer. To clarify the N-source of produced NH_3 , 0.1 M $\text{Na}^{15}\text{NO}_3$ (99 atom%) solution was used as an electrolyte instead of $\text{Na}^{14}\text{NO}_3$, and the signal of the postelectrolyte was measured using a Bruker Ascend AVANCE III 600 MHz spectrometer.

Theoretical Calculation. Spin-polarized DFT calculations were performed using the plane-wave basis Vienna ab initio simulation package (VASP) code.^{66,67} The generalized gradient approximation in the Perdew–Burke–Ernzerhof (GGA-PBE) formulation was used with a kinetic energy cutoff of 600 eV. The Gibbs free energy (ΔG) is calculated using the computational hydrogen electrode (CHE) approach and defined as^{68,69}

$$G = \Delta E_b + \Delta \text{ZPE} - T\Delta S$$

where ΔE_b is the reaction energy, ΔZPE denotes the changes of zero-point energy, and $T\Delta S$ denotes the entropy of a species. The reaction energy was calculated as

$$\Delta E_b = E_{\text{tot}} - E_{\text{molecular}} - E_{\text{adsorbate}}$$

where E_{tot} , $E_{\text{molecular}}$, and $E_{\text{adsorbate}}$ are the total energy of molecular with adsorbate, the energy of clean molecular, and the energy of adsorbate in the gas phase, respectively.

■ ASSOCIATED CONTENT

Supporting Information

The Supporting Information is available free of charge at <https://pubs.acs.org/doi/10.1021/acscatal.2c03219>.

Additional XPS, SEM, TEM, Raman, HRTEM, PDFs, online gas products analysis, chronoamperometry data,

EIS curves, CV curves, ECSA normalized LSV and NH_3 yield rate, calibration curves of HN_3 and NO_2^- , performance of graphite, CB, NTCDA-annealed, PTCDA-LIGs with different ID/IG, PQ-LIGs with different oxygen content, structures of all intermediates on G-66 and G-57/66 sites (PDF)

AUTHOR INFORMATION

Corresponding Author

Ruquan Ye – Department of Chemistry, State Key Laboratory of Marine Pollution, City University of Hong Kong, Hong Kong SAR 999077, China; City University of Hong Kong Shenzhen Research Institute, Shenzhen, Guangdong 518057, China; orcid.org/0000-0002-2543-9090; Email: ruquanye@cityu.edu.hk

Authors

Le Cheng – Department of Chemistry, State Key Laboratory of Marine Pollution, City University of Hong Kong, Hong Kong SAR 999077, China

Tinghao Ma – School of Chemistry and Chemical Engineering, Northwestern Polytechnical University, Xi'an 710072, China

Binghao Zhang – Department of Physics, City University of Hong Kong, Hong Kong SAR 999077, China

Libei Huang – Department of Chemistry, State Key Laboratory of Marine Pollution, City University of Hong Kong, Hong Kong SAR 999077, China

Weihua Guo – Department of Chemistry, State Key Laboratory of Marine Pollution, City University of Hong Kong, Hong Kong SAR 999077, China

Feijun Hu – Department of Chemistry, State Key Laboratory of Marine Pollution, City University of Hong Kong, Hong Kong SAR 999077, China

He Zhu – Department of Physics, City University of Hong Kong, Hong Kong SAR 999077, China

Zhaoyu Wang – Shenzhen Institute of Aggregate Science and Technology, School of Science and Engineering, The Chinese University of Hong Kong, Shenzhen, Guangdong 518172, China; orcid.org/0000-0002-8453-643X

Tingting Zheng – School of Materials and Energy, University of Electronic Science and Technology of China, Chengdu 610000, China

Deng-Tao Yang – School of Chemistry and Chemical Engineering, Northwestern Polytechnical University, Xi'an 710072, China; orcid.org/0000-0002-8315-5467

Chi-Kit Siu – Department of Chemistry, State Key Laboratory of Marine Pollution, City University of Hong Kong, Hong Kong SAR 999077, China; orcid.org/0000-0002-1162-6899

Qi Liu – Department of Physics, City University of Hong Kong, Hong Kong SAR 999077, China; orcid.org/0000-0003-4879-1537

Yang Ren – Department of Physics, City University of Hong Kong, Hong Kong SAR 999077, China; X-Ray Science Division, Argonne National Laboratory, Argonne, Illinois 60439, United States; orcid.org/0000-0001-9831-6035

Chuan Xia – School of Materials and Energy, University of Electronic Science and Technology of China, Chengdu 610000, China; orcid.org/0000-0003-4526-159X

Ben Zhong Tang – Shenzhen Institute of Aggregate Science and Technology, School of Science and Engineering, The Chinese University of Hong Kong, Shenzhen, Guangdong 518172, China; orcid.org/0000-0002-0293-964X

Complete contact information is available at: <https://pubs.acs.org/10.1021/acscatal.2c03219>

Notes

The authors declare no competing financial interest.

ACKNOWLEDGMENTS

The study is partially supported by the Young Scientists Fund of the National Natural Science Foundation of China (Project No. 21905240) and the Shenzhen Virtual University Park (Project No. 2021Svup129). R.Y. also acknowledges the support from the Chow Sang Sang Group Research Fund (Project No. 9229060) sponsored by Chow Sang Sang Holdings International Limited and CityU Applied Research Grant (Project No. 9667224). This research used resources of the Advanced Photon Source, a U.S. Department of Energy (DOE) Office of Science User Facility, operated for the DOE Office of Science by Argonne National Laboratory under contract no. DE-AC02-06CH11357.

REFERENCES

- (1) Ascott, M. J.; Gooddy, D. C.; Wang, L.; Stuart, M. E.; Lewis, M. A.; Ward, R. S.; Binley, A. M. Global Patterns of Nitrate Storage in the Vadose Zone. *Nat. Commun.* **2017**, *8* (1), 1416.
- (2) Abascal, E.; Gómez-Coma, L.; Ortiz, I.; Ortiz, A. Global Diagnosis of Nitrate Pollution in Groundwater and Review of Removal Technologies. *Sci. Total Environ.* **2022**, *810*, 152233.
- (3) Jia, R.; Wang, Y.; Wang, C.; Ling, Y.; Yu, Y.; Zhang, B. Boosting Selective Nitrate Electroreduction to Ammonium by Constructing Oxygen Vacancies in TiO_2 . *ACS Catal.* **2020**, *10* (6), 3533–3540.
- (4) van Langevelde, P. H.; Katsounaros, I.; Koper, M. T. M. Electrocatalytic Nitrate Reduction for Sustainable Ammonia Production. *Joule* **2021**, *5* (2), 290–294.
- (5) Wang, Y.; Zhou, W.; Jia, R.; Yu, Y.; Zhang, B. Unveiling the Activity Origin of a Copper-based Electrocatalyst for Selective Nitrate Reduction to Ammonia. *Angew. Chem., Int. Ed.* **2020**, *59* (13), 5350–5354.
- (6) Rosca, V.; Duca, M.; de Groot, M. T.; Koper, M. T. M. Nitrogen Cycle Electrocatalysis. *Chem. Rev.* **2009**, *109* (6), 2209–2244.
- (7) Zeng, Y.; Priest, C.; Wang, G.; Wu, G. Restoring the Nitrogen Cycle by Electrochemical Reduction of Nitrate: Progress and Prospects. *Small Methods* **2020**, *4* (12), 2000672.
- (8) Smith, C.; Hill, A. K.; Torrente-Murciano, L. Current and Future Role of Haber–Bosch Ammonia in a Carbon-Free Energy Landscape. *Energy Environ. Sci.* **2020**, *13* (2), 331–344.
- (9) Guo, Y.; Zhang, R.; Zhang, S.; Zhao, Y.; Yang, Q.; Huang, Z.; Dong, B.; Zhi, C. Pd Doping-Weakened Intermediate Adsorption to Promote Electrocatalytic Nitrate Reduction on TiO_2 Nanoarrays for Ammonia Production and Energy Supply with Zinc–Nitrate Batteries. *Energy Environ. Sci.* **2021**, *14* (7), 3938–3944.
- (10) Chen, F.-Y.; Wu, Z.-Y.; Gupta, S.; Rivera, D. J.; Lambeets, S. V.; Pecaut, S.; Kim, J. Y. T.; Zhu, P.; Finfrook, Y. Z.; Meira, D. M.; King, G.; Gao, G.; Xu, W.; Cullen, D. A.; Zhou, H.; Han, Y.; Perea, D. E.; Muhich, C. L.; Wang, H. Efficient Conversion of Low-Concentration Nitrate Sources into Ammonia on a Ru-Dispersed Cu Nanowire Electrocatalyst. *Nat. Nanotechnol.* **2022**, *17* (7), 759–767.
- (11) Liu, Q.; Liu, Q.; Xie, L.; Ji, Y.; Li, T.; Zhang, B.; Li, N.; Tang, B.; Liu, Y.; Gao, S.; Luo, Y.; Yu, L.; Kong, Q.; Sun, X. High-Performance Electrochemical Nitrate Reduction to Ammonia under Ambient Conditions Using a FeOOH Nanorod Catalyst. *ACS Appl. Mater. Interfaces* **2022**, *14* (15), 17312–17318.
- (12) Li, Y.; Xiao, S.; Li, X.; Chang, C.; Xie, M.; Xu, J.; Yang, Z. A Robust Metal-Free Electrocatalyst for Nitrate Reduction Reaction to Synthesize Ammonia. *Mater. Today Phys.* **2021**, *19*, 100431.
- (13) Kuang, P.; Natsui, K.; Einaga, Y. Comparison of Performance between Boron-Doped Diamond and Copper Electrodes for Selective

Nitrogen Gas Formation by the Electrochemical Reduction of Nitrate. *Chemosphere* **2018**, *210*, 524–530.

(14) Ding, J.; Li, W.; Zhao, Q.-L.; Wang, K.; Zheng, Z.; Gao, Y.-Z. Electroreduction of Nitrate in Water: Role of Cathode and Cell Configuration. *Chem. Eng. J.* **2015**, *271*, 252–259.

(15) Toh, C.-T.; Zhang, H.; Lin, J.; Mayorov, A. S.; Wang, Y.-P.; Orofeo, C. M.; Ferry, D. B.; Andersen, H.; Kakenov, N.; Guo, Z.; Abidi, I. H.; Sims, H.; Suenaga, K.; Pantelides, S. T.; Özyilmaz, B. Synthesis and Properties of Free-Standing Monolayer Amorphous Carbon. *Nature* **2020**, *577* (7789), 199–203.

(16) Hong, S.; Lee, C.-S.; Lee, M.-H.; Lee, Y.; Ma, K. Y.; Kim, G.; Yoon, S. I.; Ihm, K.; Kim, K.-J.; Shin, T. J.; Kim, S. W.; Jeon, E.-c.; Jeon, H.; Kim, J.-Y.; Lee, H.-I.; Lee, Z.; Antidormi, A.; Roche, S.; Chhowalla, M.; Shin, H.-J.; Shin, H. S. Ultralow-Dielectric-Constant Amorphous Boron Nitride. *Nature* **2020**, *582* (7813), 511–514.

(17) Li, F. C.; Liu, T.; Zhang, J. Y.; Shuang, S.; Wang, Q.; Wang, A. D.; Wang, J. G.; Yang, Y. Amorphous–Nanocrystalline Alloys: Fabrication, Properties, and Applications. *Mater. Today Adv.* **2019**, *4*, 100027.

(18) Mayorov, A. S.; Gorbachev, R. V.; Morozov, S. V.; Britnell, L.; Jalil, R.; Ponomarenko, L. A.; Blake, P.; Novoselov, K. S.; Watanabe, K.; Taniguchi, T.; Geim, A. K. Micrometer-Scale Ballistic Transport in Encapsulated Graphene at Room Temperature. *Nano Lett.* **2011**, *11* (6), 2396–2399.

(19) Sun, Y.; Liang, Y.; Luo, M.; Lv, F.; Qin, Y.; Wang, L.; Xu, C.; Fu, E.; Guo, S. Defects and Interfaces on Pt/Pb Nanoplates Boost Fuel Cell Electrocatalysis. *Small* **2018**, *14* (3), 1702259.

(20) Anantharaj, S.; Noda, S. Amorphous Catalysts and Electrochemical Water Splitting: An Untold Story of Harmony. *Small* **2020**, *16* (2), 1905779.

(21) He, Y.; Liu, L.; Zhu, C.; Guo, S.; Golani, P.; Koo, B.; Tang, P.; Zhao, Z.; Xu, M.; Zhu, C.; Yu, P.; Zhou, X.; Gao, C.; Wang, X.; Shi, Z.; Zheng, L.; Yang, J.; Shin, B.; Arbiol, J.; Duan, H.; Du, Y.; Heggen, M.; Dunin-Borkowski, R. E.; Guo, W.; Wang, Q. J.; Zhang, Z.; Liu, Z. Amorphizing Noble Metal Chalcogenide Catalysts at the Single-Layer Limit Towards Hydrogen Production. *Nat. Catal.* **2022**, *5* (3), 212–221.

(22) Zhang, X.; Luo, Z.; Yu, P.; Cai, Y.; Du, Y.; Wu, D.; Gao, S.; Tan, C.; Li, Z.; Ren, M.; Osipowicz, T.; Chen, S.; Jiang, Z.; Li, J.; Huang, Y.; Yang, J.; Chen, Y.; Ang, C. Y.; Zhao, Y.; Wang, P.; Song, L.; Wu, X.; Liu, Z.; Borgna, A.; Zhang, H. Lithiation-Induced Amorphization of Pd₃P₂S₈ for Highly Efficient Hydrogen Evolution. *Nat. Catal.* **2018**, *1* (6), 460–468.

(23) Yang, N.; Cheng, H.; Liu, X.; Yun, Q.; Chen, Y.; Li, B.; Chen, B.; Zhang, Z.; Chen, X.; Lu, Q.; Huang, J.; Huang, Y.; Zong, Y.; Yang, Y.; Gu, L.; Zhang, H. Amorphous/Crystalline Hetero-Phase Pd Nanosheets: One-Pot Synthesis and Highly Selective Hydrogenation Reaction. *Adv. Mater.* **2018**, *30* (39), 1803234.

(24) Wang, Y.; Li, H.; Zhou, W.; Zhang, X.; Zhang, B.; Yu, Y. J. A. C. Structurally Disordered RuO₂ Nanosheets with Rich Oxygen Vacancies for Enhanced Nitrate Electroreduction to Ammonia. *Angew. Chem. Int. Ed.* **2022**, *134* (19), e202202604.

(25) Geim, A. K. Graphene: Status and Prospects. *Science* **2009**, *324* (5934), 1530.

(26) Novoselov, K. S.; Geim, A. K.; Morozov, S. V.; Jiang, D.; Zhang, Y.; Dubonos, S. V.; Grigorieva, I. V.; Firsov, A. A. Electric Field Effect in Atomically Thin Carbon Films. *Science* **2004**, *306* (5696), 666.

(27) Li, X.; Magnuson, C. W.; Venugopal, A.; Tromp, R. M.; Hannon, J. B.; Vogel, E. M.; Colombo, L.; Ruoff, R. S. Large-Area Graphene Single Crystals Grown by Low-Pressure Chemical Vapor Deposition of Methane on Copper. *J. Am. Chem. Soc.* **2011**, *133* (9), 2816–2819.

(28) Tai, L.; Zhu, D.; Liu, X.; Yang, T.; Wang, L.; Wang, R.; Jiang, S.; Chen, Z.; Xu, Z.; Li, X. Direct Growth of Graphene on Silicon by Metal-Free Chemical Vapor Deposition. *Nano-Micro Lett.* **2018**, *10* (2), 20.

(29) Hernandez, Y.; Nicolosi, V.; Lotya, M.; Blighe, F. M.; Sun, Z.; De, S.; McGovern, I. T.; Holland, B.; Byrne, M.; Gun'Ko, Y. K.;

Boland, J. J.; Niraj, P.; Duesberg, G.; Krishnamurthy, S.; Goodhue, R.; Hutchison, J.; Scardaci, V.; Ferrari, A. C.; Coleman, J. N. High-Yield Production of Graphene by Liquid-Phase Exfoliation of Graphite. *Nat. Nanotechnol.* **2008**, *3* (9), 563–568.

(30) Coleman, J. N. Liquid-Phase Exfoliation of Nanotubes and Graphene. *Adv. Funct. Mater.* **2009**, *19* (23), 3680–3695.

(31) Chua, C. K.; Pumera, M. Chemical Reduction of Graphene Oxide: A Synthetic Chemistry Viewpoint. *Chem. Soc. Rev.* **2014**, *43* (1), 291–312.

(32) Yin, K.; Li, H.; Xia, Y.; Bi, H.; Sun, J.; Liu, Z.; Sun, L. Thermodynamic and Kinetic Analysis of Lowtemperature Thermal Reduction of Graphene Oxide. *Nano-Micro Lett.* **2011**, *3* (1), 51–55.

(33) Lin, J.; Peng, Z.; Liu, Y.; Ruiz-Zepeda, F.; Ye, R.; Samuel, E. L. G.; Yacaman, M. J.; Jakobson, B. I.; Tour, J. M. Laser-Induced Porous Graphene Films from Commercial Polymers. *Nat. Commun.* **2014**, *5* (1), 5714.

(34) Ye, R.; James, D. K.; Tour, J. M. Laser-Induced Graphene: From Discovery to Translation. *Adv. Mater.* **2019**, *31* (1), 1803621.

(35) Ye, R.; James, D. K.; Tour, J. M. Laser-Induced Graphene. *Acc. Chem. Res.* **2018**, *51* (7), 1609–1620.

(36) Chyan, Y.; Ye, R.; Li, Y.; Singh, S. P.; Arnusch, C. J.; Tour, J. M. Laser-Induced Graphene by Multiple Lasing: Toward Electronics on Cloth, Paper, and Food. *ACS Nano* **2018**, *12* (3), 2176–2183.

(37) Ye, R.; Chyan, Y.; Zhang, J.; Li, Y.; Han, X.; Kittrell, C.; Tour, J. M. Laser-Induced Graphene Formation on Wood. *Adv. Mater.* **2017**, *29* (37), 1702211.

(38) Zhang, Z.; Song, M.; Hao, J.; Wu, K.; Li, C.; Hu, C. Visible Light Laser-Induced Graphene from Phenolic Resin: A New Approach for Directly Writing Graphene-based Electrochemical Devices on Various Substrates. *Carbon* **2018**, *127*, 287–296.

(39) Singh, S. P.; Li, Y.; Zhang, J.; Tour, J. M.; Arnusch, C. J. Sulfur-Doped Laser-Induced Porous Graphene Derived from Polysulfone-Class Polymers and Membranes. *ACS Nano* **2018**, *12* (1), 289–297.

(40) Huang, L.; Xu, S.; Wang, Z.; Xue, K.; Su, J.; Song, Y.; Chen, S.; Zhu, C.; Tang, B. Z.; Ye, R. Self-Reporting and Photothermally Enhanced Rapid Bacterial Killing on a Laser-Induced Graphene Mask. *ACS Nano* **2020**, *14* (9), 12045–12053.

(41) Huang, L.; Gu, M.; Wang, Z.; Tang, T. W.; Zhu, Z.; Yuan, Y.; Wang, D.; Shen, C.; Tang, B. Z.; Ye, R. Highly Efficient and Rapid Inactivation of Coronavirus on Non-Metal Hydrophobic Laser-Induced Graphene in Mild Conditions. *Adv. Funct. Mater.* **2021**, *31* (24), 2101195.

(42) Stanford, M. G.; Yang, K.; Chyan, Y.; Kittrell, C.; Tour, J. M. Laser-Induced Graphene for Flexible and Embeddable Gas Sensors. *ACS Nano* **2019**, *13* (3), 3474–3482.

(43) Tao, L.-Q.; Tian, H.; Liu, Y.; Ju, Z.-Y.; Pang, Y.; Chen, Y.-Q.; Wang, D.-Y.; Tian, X.-G.; Yan, J.-C.; Deng, N.-Q.; Yang, Y.; Ren, T.-L. An Intelligent Artificial Throat with Sound-Sensing Ability based on Laser Induced Graphene. *Nat. Commun.* **2017**, *8* (1), 14579.

(44) Huang, L.; Su, J.; Song, Y.; Ye, R. Laser-Induced Graphene: En Route to Smart Sensing. *Nano-Micro Lett.* **2020**, *12* (1), 157.

(45) Ren, M.; Zhang, J.; Tour, J. M. Laser-Induced Graphene Synthesis of Co₃O₄ in Graphene for Oxygen Electrocatalysis and Metal-Air Batteries. *Carbon* **2018**, *139*, 880–887.

(46) Zhang, J.; Ren, M.; Li, Y.; Tour, J. M. In Situ Synthesis of Efficient Water Oxidation Catalysts in Laser-Induced Graphene. *ACS Energy Lett.* **2018**, *3* (3), 677–683.

(47) Peng, Z.; Ye, R.; Mann, J. A.; Zakhidov, D.; Li, Y.; Smalley, P. R.; Lin, J.; Tour, J. M. Flexible Boron-Doped Laser-Induced Graphene Microsupercapacitors. *ACS Nano* **2015**, *9* (6), 5868–5875.

(48) Ferrari, A. C.; Meyer, J. C.; Scardaci, V.; Casiraghi, C.; Lazzeri, M.; Mauri, F.; Piscanec, S.; Jiang, D.; Novoselov, K. S.; Roth, S.; Geim, A. K. Raman Spectrum of Graphene and Graphene Layers. *Phys. Rev. Lett.* **2006**, *97* (18), 187401.

(49) Malard, L. M.; Pimenta, M. A.; Dresselhaus, G.; Dresselhaus, M. S. Raman Spectroscopy in Graphene. *Phys. Rep.* **2009**, *473* (5), 51–87.

- (50) Huang, C.-H.; Lin, H.-Y.; Huang, C.-W.; Liu, Y.-M.; Shih, F.-Y.; Wang, W.-H.; Chui, H.-C. Probing Substrate Influence on Graphene by Analyzing Raman Lineshapes. *Nanoscale Res. Lett.* **2014**, *9* (1), 64.
- (51) Yan, Z.; Liu, Y.; Ju, L.; Peng, Z.; Lin, J.; Wang, G.; Zhou, H.; Xiang, C.; Samuel, E. L. G.; Kittrell, C.; Artyukhov, V. I.; Wang, F.; Yakobson, B. I.; Tour, J. M. Large Hexagonal Bi- and Trilayer Graphene Single Crystals with Varied Interlayer Rotations. *Angew. Chem., Int. Ed.* **2014**, *126* (6), 1591–1595.
- (52) Amato, G.; Milano, G.; Vignolo, U.; Vittone, E. Kinetics of Defect Formation in Chemically Vapor Deposited (CVD) Graphene During Laser Irradiation: The Case of Raman Investigation. *Nano Res.* **2015**, *8* (12), 3972–3981.
- (53) Unwin, P. J.; Onoufriou, D.; Jones, T. S. Growth and Vibrational Properties of PTCDA Thin Films on InSb(111)A. *Surf. Sci.* **2003**, *547* (1), 45–54.
- (54) Zou, Y.; Kilian, L.; Schöll, A.; Schmidt, T.; Fink, R.; Umbach, E. Chemical Bonding of PTCDA on Ag Surfaces and the Formation of Interface States. *Surf. Sci.* **2006**, *600* (6), 1240–1251.
- (55) Minnekhanov, A. A.; Deygen, D. M.; Konstantinova, E. A.; Vorontsov, A. S.; Kashkarov, P. K. Paramagnetic Properties of Carbon-Doped Titanium Dioxide. *Nanoscale Res. Lett.* **2012**, *7* (1), 333.
- (56) Gong, Z.; Zhong, W.; He, Z.; Liu, Q.; Chen, H.; Zhou, D.; Zhang, N.; Kang, X.; Chen, Y. Regulating Surface Oxygen Species on Copper (I) Oxides via Plasma Treatment for Effective Reduction of Nitrate to Ammonia. *Appl. Catal., B* **2022**, *305*, 121021.
- (57) Ćirić, L.; Sienkiewicz, A.; Gaál, R.; Jaćimović, J.; Văju, C.; Magrez, A.; Forró, L. Defects and Localization in Chemically-Derived Graphene. *Phys. Rev. B* **2012**, *86* (19), 195139.
- (58) Diamantopoulou, A.; Glenis, S.; Zolnierkiwicz, G.; Guskos, N.; Likodimos, V. Magnetism in Pristine and Chemically Reduced Graphene Oxide. *J. Appl. Phys.* **2017**, *121* (4), 043906.
- (59) Cançado, L. G.; Takai, K.; Enoki, T.; Endo, M.; Kim, Y. A.; Mizusaki, H.; Jorio, A.; Coelho, L. N.; Magalhães-Paniago, R.; Pimenta, M. A. General Equation for the Determination of the Crystallite Size L_a of Nanographite by Raman Spectroscopy. *Appl. Phys. Lett.* **2006**, *88* (16), 163106.
- (60) Ganz, E.; Ganz, A. B.; Yang, L.-M.; Dornfeld, M. The Initial Stages of Melting of Graphene between 4000 and 6000 K. *Phys. Chem. Chem. Phys.* **2017**, *19* (5), 3756–3762.
- (61) Chen, G.-F.; Yuan, Y.; Jiang, H.; Ren, S.-Y.; Ding, L.-X.; Ma, L.; Wu, T.; Lu, J.; Wang, H. Electrochemical Reduction of Nitrate to Ammonia via Direct Eight-Electron Transfer using a Copper–Molecular Solid Catalyst. *Nat. Energy* **2020**, *5* (8), 605–613.
- (62) Ye, R.; Peng, Z.; Wang, T.; Xu, Y.; Zhang, J.; Li, Y.; Nilewski, L. G.; Lin, J.; Tour, J. M. In Situ Formation of Metal Oxide Nanocrystals Embedded in Laser-Induced Graphene. *ACS Nano* **2015**, *9* (9), 9244–9251.
- (63) Liang, Y.; Li, Y.; Wang, H.; Zhou, J.; Wang, J.; Regier, T.; Dai, H. Co_3O_4 Nanocrystals on Graphene as a Synergistic Catalyst for Oxygen Reduction Reaction. *Nat. Mater.* **2011**, *10* (10), 780–786.
- (64) Zhu, D.; Zhang, L.; Ruther, R. E.; Hamers, R. J. Photo-Illuminated Diamond as a Solid-State Source of Solvated Electrons in Water for Nitrogen Reduction. *Nat. Mater.* **2013**, *12* (9), 836–841.
- (65) Green, L. C.; Wagner, D. A.; Glogowski, J.; Skipper, P. L.; Wishnok, J. S.; Tannenbaum, S. R. Analysis of Nitrate, Nitrite, and ^{15}N Nitrate in Biological Fluids. *Anal. Biochem.* **1982**, *126* (1), 131–138.
- (66) Stankovich, S.; Dikin, D. A.; Piner, R. D.; Kohlhaas, K. A.; Kleinhammes, A.; Jia, Y.; Wu, Y.; Nguyen, S. T.; Ruoff, R. S. Synthesis of Graphene-based Nanosheets via Chemical Reduction of Exfoliated Graphite Oxide. *Carbon* **2007**, *45* (7), 1558–1565.
- (67) Kresse, G.; Joubert, D. From Ultrasoft Pseudopotentials to the Projector Augmented-Wave Method. *Phys. Rev. B* **1999**, *59* (3), 1758–1775.
- (68) Rossmeisl, J.; Logadottir, A.; Nørskov, J. K. Electrolysis of Water on (Oxidized) Metal Surfaces. *Chem. Phys.* **2005**, *319* (1), 178–184.
- (69) Nørskov, J. K.; Rossmeisl, J.; Logadottir, A.; Lindqvist, L.; Kitchin, J. R.; Bligaard, T.; Jónsson, H. Origin of the Overpotential for Oxygen Reduction at a Fuel-Cell Cathode. *J. Phys. Chem. B* **2004**, *108* (46), 17886–17892.

Recommended by ACS

Ultrafast and Controllable Phase Evolution by Flash Joule Heating

Weiyin Chen, James M. Tour, *et al.*

JUNE 17, 2021
ACS NANO

READ 

Insight into the Real Efficacy of Graphene for Enhancing Photocatalytic Efficiency: A Case Study on CVD Graphene- TiO_2 Composites

Zhuquan Huang, Qingrong Qian, *et al.*

AUGUST 24, 2021
ACS APPLIED ENERGY MATERIALS

READ 

Bulk Production of Any Ratio ^{12}C : ^{13}C Turbostratic Flash Graphene and Its Unusual Spectroscopic Characteristics

Kevin M. Wyss, James M. Tour, *et al.*

JUNE 07, 2021
ACS NANO

READ 

Photo-organometallic, Nanoparticle Nucleation on Graphene for Cascaded Doping

Songwei Che, Vikas Berry, *et al.*

OCTOBER 14, 2019
ACS NANO

READ 

Get More Suggestions >